

Medial surfaces of hyperbolic structures

G.E. Schröder^{1,a}, S.J. Ramsden^{1,2}, A.G. Christy^{1,3}, and S.T. Hyde¹

¹ Dept. of Applied Maths, Research School of Physical Sciences, Australian National University, Canberra 0200 ACT, Australia

² Supercomputer Facility, Australian National University, Canberra 0200 ACT, Australia

³ Geology Department, Australian National University, Canberra 0200 ACT, Australia

Received 23 January 2003 / Received in final form 31 July 2003

Published online 24 October 2003 – © EDP Sciences, Società Italiana di Fisica, Springer-Verlag 2003

Abstract. We describe an algorithm for numerical computation of a medial surface and an associated medial graph for three-dimensional shapes bounded by oriented triangulated surface manifolds in three-dimensional Euclidean space (domains). We apply the construction to bicontinuous domain shapes found in molecular self-assemblies, the cubic infinite periodic minimal surfaces of genus three: Gyroid (G), Diamond (D) and Primitive (P) surfaces. The medial surface is the locus of centers of *maximal spheres*, *i.e.* spheres wholly contained within the domains which graze the surface tangentially and are not contained in any other such sphere. The construction of a medial surface is a natural generalization of Voronoi diagrams to continuous surfaces. The medial surface provides an explicit construction of the volume element associated with a patch of the bounding surface, leading to a robust measure of the surface to volume ratio for complex forms. It also allows for sensible definition of a line graph (the medial graph), particularly useful for domains consisting of connected channels, and not reliant on symmetries of the domains. In addition, the medial surface construction produces a length associated with any point on the surface. Variations of this length give a useful measure of global homogeneity of topologically complex morphologies. Comparison of medial surfaces for the P, D and G surfaces reveal the Gyroid to be the most globally homogeneous of these cubic bicontinuous forms (of genus three). This result is compared with the ubiquity of the G surface morphology in soft mesophases, including lyotropic liquid crystals and block copolymers.

PACS. 02.40.-k Geometry, differential geometry, and topology – 02.70.-c Computational techniques – 61.30.St Lyotropic phases – 81.05.Rm Porous materials; granular materials – 81.16.Dn Self-assembly

1 Introduction

The intent of this paper is threefold. Its primary aims are (i) to introduce an algorithm for determination of a generalised Voronoi domain for complex 3D morphologies, (ii) to define a 1D skeleton of the domains and (iii) to apply the analysis to simpler infinite triply-periodic minimal surfaces (IPMS). The work is particularly focussed on non-convex bodies with topological complexity, containing, for example, multiply inter-connected pore spaces. The concept is an extension of extant techniques in discrete computational geometry, where it is commonly referred to as the *medial (or symmetric) axis (or surface)* (MS) [10, 53].

The MS construction is useful in many contexts. First, the MS can be thought of as a generalized Voronoi partition for a surface form of arbitrary topological and geometric complexity. Voronoi analysis of morphologies consisting of spherical domains is well known; more recently it was extended to domain shapes consisting of assemblies of convex objects in 3D [45]. Here we generalise the construc-

tion to more general forms in 3D Euclidean space, applicable to complex hyperbolic geometries. In common with the usual meaning of a Voronoi partition, the patches of the MS are thus maximally distant from the original surface and play an important role in general packing problems involving complex shapes. For example, the MS is a generalisation of confocal domains, relevant to lamellar or smectic liquid crystals [41]. In a related context, the MS geometry may afford a better model for “chaotic zones” of liquid crystalline mesophases in lipid-water systems, introduced by Luzzati [46].

Second, by analogy with the Voronoi construction, the MS construction allows for calculation of the volumes on either side of the original surface associated with a surface patch. Robust definitions of the surface to volume ratio of a surface patch, and its variations over a complete surface, are therefore possible (and described in detail later in the paper).

Third, the medial surface can be used as a basis for construction of a one-dimensional *medial graph* that characterises channel axes and channel connectivity for complex porous morphologies. The concept of channel graphs

^a e-mail: Gerd.Schroeder@anu.edu.au

has been widely used to describe the global geometry and topology of IPMS, following Schoen's description of the "labyrinth graph" defining the channel geometry of various IPMS [59]. In quite a different context, quantification of channel axes in random porous media is needed for calculations of fluid transport as a function of morphology [8,65]. Here we introduce a rigorous numerical algorithm for the medial graph, applicable to triangulated surfaces, and demonstrate the fragility of this construction, that—in contrast to the medial surface transform—generally does not allow for unique surface reconstruction.

We apply the algorithm to three cubic triply periodic minimal surfaces. The relevance of these forms to condensed molecular self-assemblies, particularly bicontinuous mesophases of lyotropic liquid crystals and block copolymers is well documented [35,36,56,61]. We show later that the construction of medial surfaces in these cases may shed light on unresolved questions concerning the relative stability of bicontinuous mesophases.

The remainder of this article is organized as follows: In Section 2 a definition of the medial surface is given and some of its properties are outlined. Section 3 describes our MS algorithm and illustrates it with the IPMS mentioned above. Section 4 deals with the reduction of the medial surface to a medial graph, and Section 5 gives an analysis of the distance function for the P, D and G surfaces. We conclude by mentioning some future directions.

2 Definition and properties of medial surfaces

We define a *domain* C as an open, connected subset of \mathbb{E}^3 whose boundary ("skin"), $S = \partial C$, is an oriented piecewise smooth manifold, or a set of piecewise smooth manifolds. For example, a domain might be one of the two subvolumes bounded by an IPMS, the void or the solid phase of a porous medium, a three-dimensional solid, or the complement of a set of disjoint solid objects.

The boundary surface of a domain is always orientable, and has a piecewise smooth normal field N defined everywhere on S . The normal field along edges and vertices is defined by replacing edges by a cylindrical surface element and vertices by a spherical cap, both of vanishingly small radius. We assume the surface normals are of unit length and oriented to point into the domain C .

In a very loose sense, the MS defines the "centre" of a domain. That idea is quantified by the following definition: The medial surface MS of the domain C is the locus of centers of all maximal spheres in C , *i.e.* those spheres contained in C which are not contained in any other sphere in C [10,52]. Equivalently, the medial surface is the set of points in C with more than one nearest neighbour on the domain boundary S .

The medial surface of a domain generally consists of a collection of surface patches meeting along one-dimensional curves. In particular cases, the patches may extend to infinity, or degenerate to one-dimensional curves or even points. If S has a convex edge (or vertex), *i.e.* a line (point) where the normal field is discontinuous and

the corner is pointing out of the domain, then there is a MS patch extending up into the corners of the surface.

Some examples clarify the features of the medial surface construction. The medial surface of an infinite slab of thickness d (bounded by two parallel planes) is a parallel plane at distance $d/2$ in between the two original planes. The medial surface of a sphere is its center point, and the medial surface of a cylinder with circular cross section is its rotational symmetry axis. The medial surface of a straight cylinder along the z -axis whose cross section is the ellipse given by $(x/a)^2 + (y/b)^2 = 1$ with $a > b$ is a flat ribbon $\{(x, 0, z) \mid -\infty \leq z \leq \infty, |x| \leq a - b^2/a\}$ in the $y = 0$ plane.

Any point $p \in S$ on the boundary S of a domain C has exactly one corresponding point $q := ms(p)$ on the medial surface MS of C (The converse is not true.) The point p is located at the shortest distance from q compared with all other points on S . Therefore the map ms from a point on S to the corresponding medial surface point can be written as

$$ms : S \rightarrow \mathbb{E}^3, \quad p \mapsto ms(p) := p + d(p)N(p) \quad (1)$$

where N is the normal field of S and $d : S \rightarrow \mathbb{R}^+$ is called the distance (or radius) function.

The distance function $d : S \rightarrow \mathbb{R}^+$ is formally similar to the radius of curvature $r_c : S \rightarrow \mathbb{R}^+$ in that both measure distances in the normal direction from points on the surface.

In general, at any given point $p \in S$ there exist two distinct radii of curvature $r_{c,1}$ and $r_{c,2}$ corresponding to the two principal directions on S . Only curvature towards N can lead to curvature induced points of the MS in positive normal direction. We therefore define r_c as the minimum of the positive radii of curvature and infinity, and T_c as the corresponding principal direction.

Indeed, the maximal sphere K_m centered at $ms(p)$ with radius $d(p)$ and the sphere K_r centered at the center of curvature $p + r_c(p)N(p)$ with radius $r_c(p)$ are both tangential to S in p . By definition, K_m is contained in C (global). In contrast, K_r need not be contained in C . Rather, restricted to the normal section P_n of S that contains the principal direction T_c , the circle $K_r \cap P_n$ is an osculating circle to the flat curve $S \cap P_n$.

It is straightforward to see that $d(p) \leq r_c(p)$ for all $p \in S$: Assume there exists a sphere K whose radius exceeds r_c , which grazes S at p and lies in positive normal direction from p . The sphere K contains K_r . But K_r coincides with S in a neighbourhood of p along at least one direction. Therefore, a finite part of S is contained in K . Thus K cannot be a maximal sphere.

More precisely, a unit speed space curve α coincident with the intersection of S with the plane containing the normal $N(p)$ and the principal direction $T_c(p)$ has curvature $1/r_c$ at the point p . Also the surface normal $N(p)$ is identical to the curve normal (see *e.g.* Corollary 16.8 in [27]). A finite part of this curve is contained in the larger sphere K with $r > r_c$, because α curves more strongly towards $N(p)$ than does K . Therefore, K cannot be a maximal sphere contained in C .

The medial surface can also be described as the cut locus of the normal bundle of the surface [72], which in turn corresponds to singularities of the parallel surface transform of S . In other words, the MS corresponds to the locus of points of self-intersection of the foliation of parallel surfaces generated by translating all points on the surface a distance x along their normal, where x varies from 0 (the original surface) to some upper translation distance, $d(p)$ (in fact, this construction was already described by Lord Kelvin [44] in 1894). This interpretation allows for a useful association of a surface element $da(p)$ to a *volume element* $dV(p)$ which is the union of all parallel surface elements $da(p, x)$ of $da(p)$ with distances $x \leq d(p)$.

The medial surface accurately represents the topology of the original domain, in the sense that the MS is a strong deformation retract (see [66] for a definition) of the original domain C in $2d$ [12], and in $3d$ provided S is smooth [72]. That means that, though the dimension of C is in general different to that of the MS, they have the same tunnels, holes and connected components.

Furthermore, the medial surface together with the distance function d allows for the reconstruction of the domain C as the union of the maximal spheres of radius $d'(ms(p)) = d(p)$ centered at the medial surface points $ms(p)$ [72].

It is useful to classify points q on the MS according to their order, *i.e.* the number of disjoint subsets of the set of points $p' \in S = \partial C$ with $ms(p') = q$ [10, 52, 72]. Points on branch lines of the MS are of order 3 or more, and points on the boundary of MS patches have order 1. *Normal* points contained within MS patches and not on the boundary or at a branch line have order 2.

Provided S is C^2 , MS points p^* of order 1 are centers of curvature of S (Theorem 3 in [72]). This means that the boundaries of the MS are also part of the focal surface of S given by equation (1) with $d(p^*)$ replaced by $r_c(p^*)$. It is a standard result from differential geometry that cusp lines of the focal surfaces correspond to ridge lines of $1/r_c$ on S (*i.e.* points $p \in S$ such that for each point the directional derivative of r_c vanishes in one direction) provided S is free of non-flat umbilic points [27]. Boundaries of the medial surface – order 1 points – are cusp lines of the focal surface, see [26] and references therein.

The medial surface construction implies sensitivity to the normal field of the boundary $S = \partial C$ of the domain C and higher order measures dependent on that field, such as the surface curvatures. Perturbations of the original domain under which the medial surface changes continuously must involve only small changes in the normal field of S . In particular, the condition that the Hausdorff-distance (see *e.g.* [57]) between two domains C and C' is small, is not sufficient to guarantee small differences in Hausdorff-distance between the medial surfaces of C and C' [13, 14, 62]. Most importantly, the medial surface of a domain bounded by a smooth manifold S and that bounded by a faceted surface approximating S differ strongly from each other: the MS of the faceted domain has MS patches extending into all facet edges and corners. Those differences reflect real differences in the

curvatures of the smooth manifold, and that of its faceted analogue. The sensitivity to variation of normals and curvatures is inherent to the medial surface transform and not due to the algorithmic details of its computation.

The presence of short-wavelength modulations of the boundary surface S , inducing high surface curvatures, complicate the branching structure and topology of the medial surface. Extraction of global features of the MS, that are characteristic of the relative disposition of surface elements in space, rather than local curvatures, requires imposition of a suitably chosen curvature cutoff prior to analysis of the domain. That can be done, for example, by imposing a “rolling ball” filter on S , whose radius sets the maximum surface curvatures [68, 69].

Finally, the distance function d is always continuous [72] but not necessarily C^1 . This fact is of some importance for our reduction of a medial surface to a medial graph to be described later in this paper. Two $2D$ examples clarify the problem: (1) The MS of an equilateral triangle are three branches connecting the incircle center to the three corner points. The distance function d is not smooth at the mid-edges of the triangle which correspond to the incircle center on MS . (2) A rhombus whose flat corners are replaced by segments of circles has a discontinuity in the derivative of d at the point where the straight lines and circle segments meet (note that the rhombus is smooth even there).

3 MS algorithm for triangulated domains

This section describes a Voronoi-based MS algorithm for a domain C in $3D$ Euclidean space whose boundary surface $S = \partial C$ is given as a *triangulated surface*. The MS we compute is the medial surface of the piece-wise smooth surface approximated by the triangulation. The description of the algorithm is illustrated by MS computation for the Gyroid, Diamond and Primitive IPMS, and followed by some discussions on the robustness of our algorithm.

Algorithms to compute medial surfaces of voxelized representations (discrete binary or grayscale $3D$ data sets) of surface objects in \mathbb{E}^3 based on burning techniques [43, 58] or on wave-propagation approaches [23] have been suggested. Medial surfaces of polyhedral structures (where corners and edges are explicit features of the object rather than artifacts due to discretization) can be computed [16]. Voronoi-based algorithms to compute medial surfaces of triangulated surfaces have been suggested [2, 5, 17, 63], and the algorithm we describe here is related to those, with some differences. For the examples discussed in this article, a triangulation is an ideal representation as it allows for very accurate MS computations and is, given the high resolution we achieve, modest in memory needs.

The surface S is represented by a set of points $V = \{(x, y, z) \in S\}$ and a set T of oriented triangles whose vertices are the points in V (the coordinates x , y and z are floating-point numbers). The sampling density on the surface is assumed to be sufficiently high. Furthermore, we assume that normal vectors $N_i := N(p_i)$ for all points $p_i \in V$ are given.

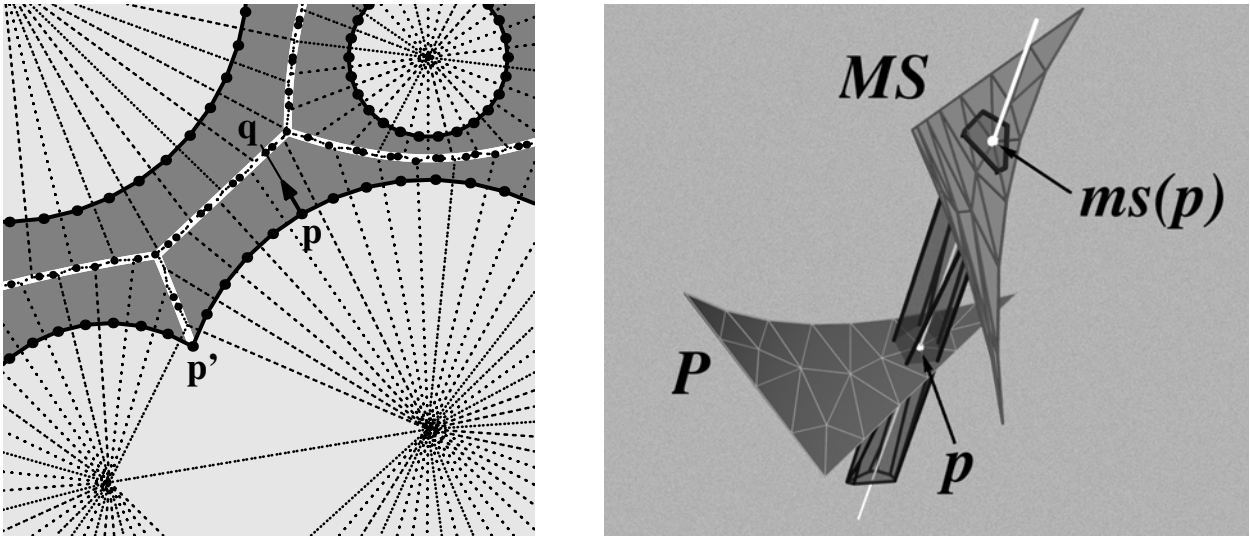


Fig. 1. (left) 2D illustration of the medial surface/axis algorithm: The domain C (dark gray) is the complement of an assembly of overlapping disks (light gray). The boundary ∂C of the domain is discretized into vertices V (black points) connected by edges. The interface normal vectors are pointing into C . The first step is the computation of the Voronoi diagram of the set of vertices V (dashed lines). For every point $p \in \partial C$ there is a corresponding point q on the medial surface which is the intersection of the straight line in normal direction through p with the Voronoi cell of p (the black points on the white line), unless p is at a cusp of ∂C . If p is at a concave cusp of ∂C (as is the vertex p'), then $ms(p) = p$. The white line is the exact medial axis, for which an analytic form is known in the case of disk assemblies [45,49]. (right) 3D case: A small patch P of the boundary $S = \partial C$ of a domain C is shown (the lower surface patch) together with its triangulation. Also shown is the Voronoi cell of a vertex p (marked by a small white point on the surface inside the cell) of the triangulation which is an elongated, convex polyhedron oriented along the surface normal direction (bounded by thick black lines, joined by opaque faces). The white line is the straight line in normal direction through p , which intersects the Voronoi cell of p at $ms(p)$ (white point). The surface patch in the top part of the image is the MS patch corresponding to P and its triangulation is inherited from P . Note that for the computation of the Voronoi diagram as a global property of C , a much larger fraction of S is needed than the patch shown.

For the examples of triply periodic minimal surfaces discussed later in the paper, the points $p \in V$ and normals can be computed to high precision by integration of the Weierstrass equations (see *e.g.* [21]). This is the ideal situation for our algorithm, which allows for very accurate analysis of the MS structure itself (*e.g.* the asymmetric unit patches of the surfaces analysed later contain approximately 10000 vertices).

The first step is the computation of the Voronoi diagram of the surface vertices V . In keeping with the usual definition (see *e.g.* [6,55]), we define the Voronoi diagram to be the division of space with respect to V into n convex cells $C_V(p) \subset \mathbb{E}^3$ such that for any point $p \in V$ any point $q \in C_V(p)$ is closer to p than to any other point $p' \in V$ (n is the number of vertices in V). See Figure 1 for an illustration.

The second step is to find (for each point $p \in V$) the point q on the faces of the Voronoi cell $C_V(p)$ which best approximates the medial surface point $ms(p)$. The key idea is that, given appropriate sampling density on S , the Voronoi cell $C_V(p)$ is an elongated cell oriented in surface normal direction $N(p)$. The medial surface point $ms(p)$ lies on one of the faces furthest away from p in normal direction.

Provided that the vertices in V are points on the exact surface S , exact coordinates of the surface normal vectors $N(p)$ are known and high precision computations are fea-

sible, the medial surface vertex $ms(p)$ for a given surface vertex p can be estimated to high precision. The vertex position is then given by the intersection of the straight line through p in direction of the surface normal $N(p)$ with the boundary of its Voronoi cell $C_V(p)$. This construction is shown in Figure 1.

If exact normals $N(p)$ are not known, this step is replaced by a more heuristic approach, that requires the imposition of two control parameters, d_1 and α .

For each surface vertex p with Voronoi cell $C_V(p)$, determine the *pole vertex* q_p , *i.e.* that vertex of $C_V(p) \cap C$ which maximizes the distance from p among all vertices $q \in C_V(p) \cap C$. Let $d(q_p)$ denote its distance from p . Then determine possible *pole faces*, *i.e.* those faces $F_i \in C_V(p)$ for which all vertices $q \in F_i$ fulfil the inequality $(d(q) - d(q_p))/d(q_p) < d_1$ and whose face normals differ from the *pole vector* $v_p = (q_p - p)$ by less than α (note that v_p is a good approximation of the surface normal vector [1]). If such pole faces exist, then $ms(p)$ is the intersection of the straight line through the centroid of the pole faces and through the surface vertex p itself with $C_V(p)$. If there are none, then $ms(p)$ is the pole vertex q_p .

Previous algorithms have approximated the medial surface of objects sampled by a point set V on their boundary through subsets of the vertices of the Voronoi diagram of the point set V [2,5,63]. Amenta *et al.* [2] and others [11] have provided proof that the set of poles converges

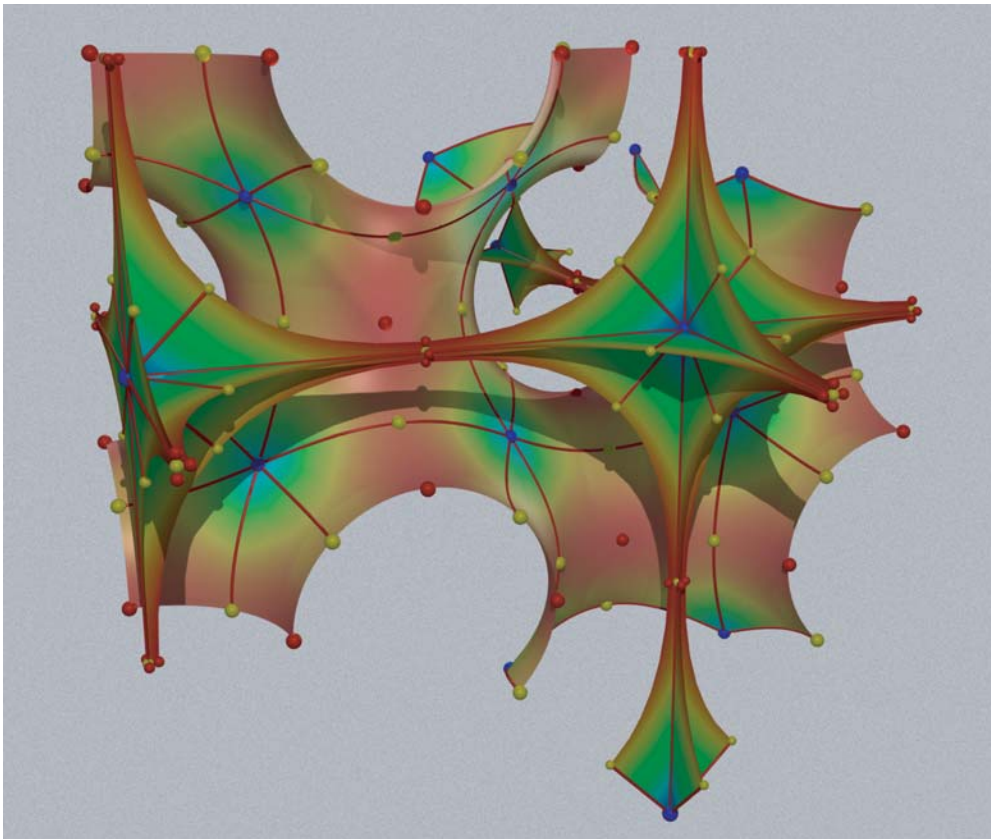


Fig. 2. Portion of a medial surface of the P(rimitive) IPMS, together with the IPMS. Both the IPMS and the MS are coloured according to values of the distance function d : red indicates small d values and blue large values. All points of the medial surface are contained in mirror planes of the P surface, and the boundary of the MS corresponds to points where the MS points are also centers of curvature, $d(p) = r_c(p)$. Red, yellow and blue spheres indicate minima, saddle points and maxima of the distance function, respectively. Note that there is only one type of maximum, *i.e.* all maxima are at equivalent position of the space group (the same is true for the minima), but that there are two crystallographically distinct saddle points: S_1 in 100 (on Schoen’s line graph) and S_2 in 110 direction from the maximum (on the MS, see also Tab. 1). The red lines on the surface are ridge lines of d connecting saddles to maxima, and the red lines on the medial surface their images under ms . The simple cubic line graph, that is the labyrinth graph of the P surface [59] is a subset of the ridge lines.

to the medial surface if the sampling density of points on S goes to infinity (whereas the set of all Voronoi vertices contained in C does not). In the limit of infinite sampling density, our algorithm produces the same result. We find that for finite sampling densities we get a better approximation of the medial surface vertices than Amenta *et al.* for data without noise and with normals that are computable to arbitrary accuracy.

In addition, the algorithm introduced here gives a better triangulation of the MS (inherited from S) than if $ms(p)$ is approximated by the pole vertex since quasi-degeneracy of pole vertices can lead to overlapping MS triangles (consider the hexagonal Voronoi cells of a set of parallel planes triangulated by unisize equilateral triangles as an example). We note that Amenta *et al.* [2] use a different technique to generate the triangulation of the MS.

For the analysis presented in this article we used Muecke’s Delaunay triangulation code ‘detri’ [51] which uses a variant of the randomized incremental-flip algorithm and a symbolic perturbation scheme to achieve ro-

bustness. From the Delaunay diagram we computed the Voronoi diagram using Shewchuk’s robust 3D predicate code [64].

Robustness of the medial surface algorithm

With regards to algorithmic stability –rather than the conceptual sensitivity discussed in Section 2– two issues need to be addressed: convergence of the algorithm for noise-free surface data with increasing sampling density, and sensitivity of the algorithm to noise. The former case arises where all points p in the sampling set V are contained in S , *i.e.* there is no positional out-of-surface noise. In the limit where the sampling becomes infinitely dense, our algorithm provides the same results as that of Amenta *et al.* [2]. Consequently, their statement that the set of poles converges to the true medial surface as the sampling density goes to infinity also guarantees the convergence of our algorithm. As in the Amenta algorithm, precise bounds on the quality of the MS approximation are difficult to deduce, but the convergence is assured (see also [11]).

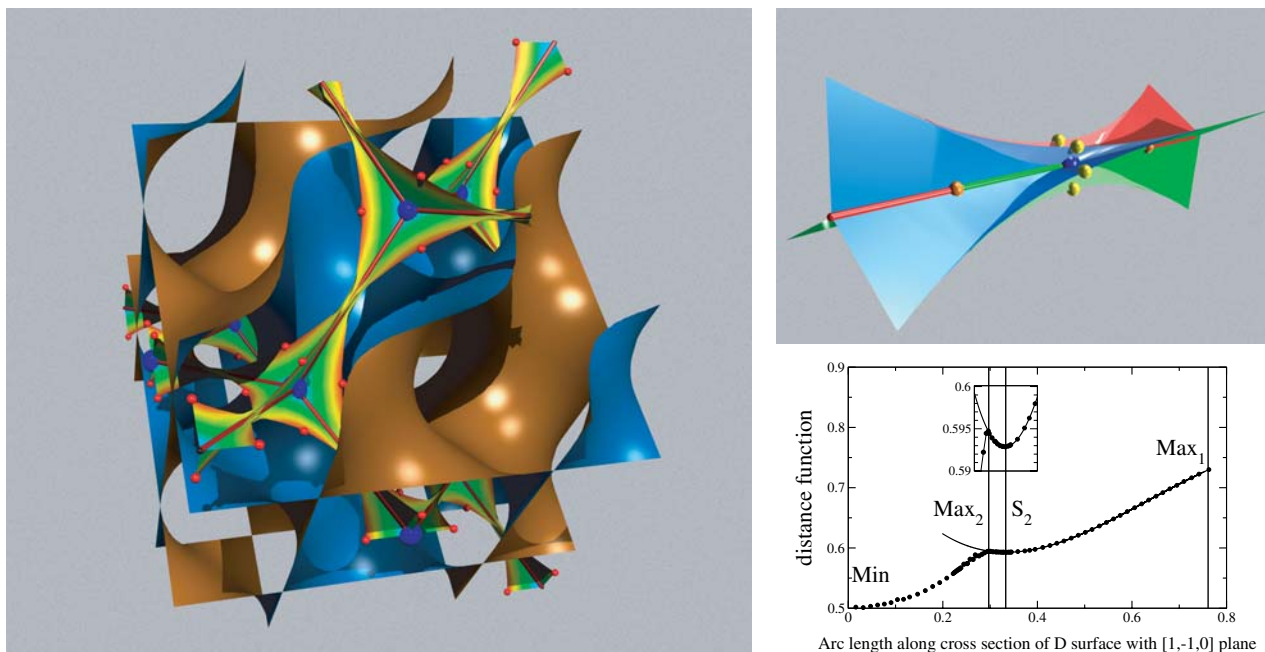


Fig. 3.

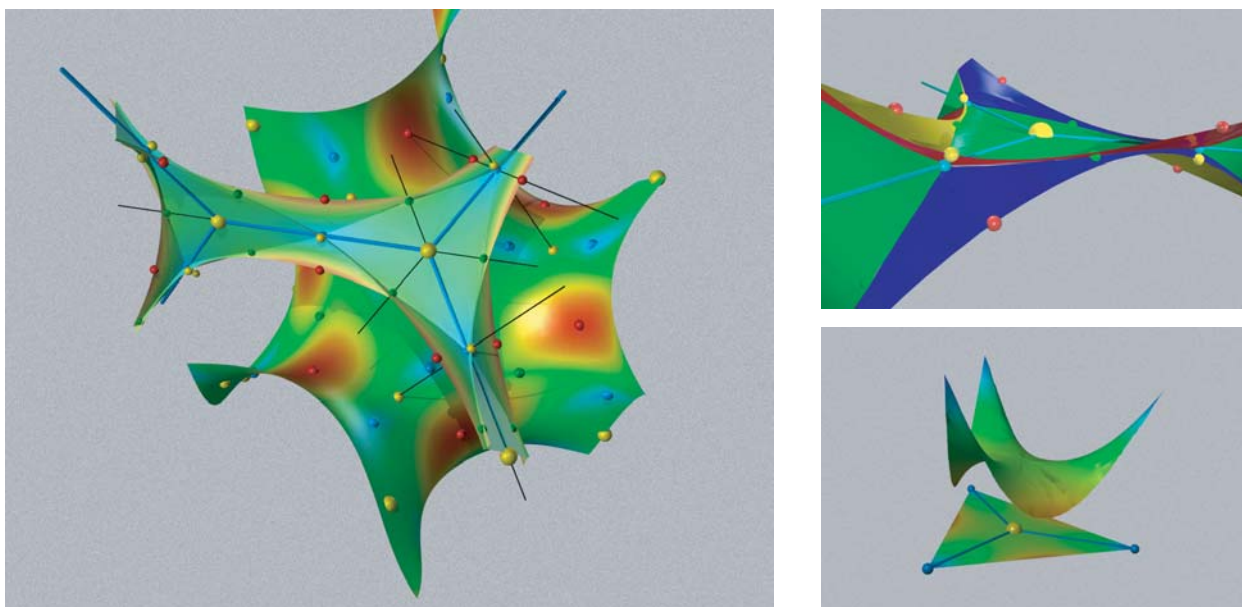


Fig. 4.

Fig. 3. Diamond IPMS: (left) A fragment of the D IPMS is shown, together with the medial surface of one of its two channel labyrinths. (The MS is coloured according to distance function as described in Fig. 2.) The red lines (along [111] directions of the corresponding space group, see Tab. 1) correspond to one of the two interpenetrating diamond lattices commonly accepted as labyrinth graphs of the D surface [59]. The blue spheres indicate the main distance function maxima located at the nodes of the line graph, and the small red spheres its minima. The MS can be approximated by an assembly of almost flat webs spanning the six pairs of graph edges (from the node to the middle of the edge) emanating from each node, and each of these webs is contained in one of the global mirror planes. The two sets of three webs meeting at the center of each graph edge subtend angles of 60° with each other. The top right image is a close-up of the MS close to the middle of a graph edge (The graph edges are on three-fold symmetry axes with inversion centers at their centers, the blue spheres. Each of the yellow spheres S_1 lies on a two-fold axis through this inversion center.) The medial surface webs do not shrink to a single point (as one moves along the graph edge), but rather each of the webs splits up into two webs (at $\pm 60^\circ$). It is only in this region that the MS is not contained within global mirror planes of the surface. The yellow and green spheres indicate saddle points of the distance function, and the blue sphere a very weak maximum of the distance function. Critical paths connect the node max Max_1 to the saddle S_2 on the edge (red line), S_2 to Max_2 (green line) and each of the six yellow S_1 to Max_2 (not shown). The graph shows the distance function on a $(1\bar{1}0)$ plane intersection of S (*i.e.* the mirror plane relating the two blue planes). It corresponds to distance function values on the line graph on MS). Dots are data computed with our algorithm, whereas the full curve is the length of lines directed along surface normals between the surface vertices and the global mirror planes. This latter procedure yields exact distance values for the region from the graph nodes to the edge center, clearly demonstrating that the blue sphere is indeed a weak maximum and the orange sphere a saddle point.

Fig. 4. Medial surface of the G(yroid) triply periodic minimal surface coloured according to the scheme described in Figure 2. The thin black lines are some of the two-fold rotational symmetry axes of the G surface. The conventional labyrinth graph (blue thick lines) for the G surface connects nearest pairs of points of intersection of these two-fold axes through straight lines [59]. These are a subset of the ridge lines of the distance function, though, in contrast to the P and D surfaces, the nodes of the channel graph are not the maxima of the distance function (the maxima, blue spheres, are in the middle of the edges). There are three different types of saddle points of the distance function: saddle singularities of Hopf index -2 at the nodes of the graph (large yellow spheres, S_1 , as well as two types S_2 (small yellow spheres) and S_3 (green) of saddle singularities of Hopf index -1 . The critical paths connecting S_3 to the maximum and S_2 to the maximum are not shown. The top right image (with arbitrary color coding) illustrates that the medial surface is an assembly of nearly planar triangles (green) plus *webs* spanned between the edges of neighbouring triangles. Pairs of adjacent triangles share common vertices and are twisted by $\cos^{-1}(1/3) \approx 70.53^\circ$ around the common two-fold rotational axis containing the the labyrinth graph, consistent with symmetries of the G surface. Numerical results indicate that the triangular portions of the MS deviate from planarity by only $\pm 0.75\%$ of the triangle edge length. (bottom right) One of the triangles of the MS with the saddle point in its center and three maxima located at each of its corners beneath a surface graph whose height indicates the value of the distance function at the site immediately below, on the projected triangle.

Sampling noise, particularly out-of-surface noise, affects the normal field of the bounding surface S . Our algorithm, like earlier ones, is therefore susceptible to surface roughness at the length scale of the typical triangle edge length since it requires an accurate estimate of the variation of surface normals and derivatives, such as curvatures. It is clear that our algorithm gives a good approximation of the true MS if the surface normals computed from the triangulation are a good approximation of the true surface normals. For example, Figure 5 demonstrates that our algorithm can cope with small levels of (positional) noise in the case of an ellipsoid (see Sect. 5 for a definition of the distance distribution). Evidently, a small degree of orientational randomness does not affect the results significantly. Further, precise knowledge of surface normals makes only a small difference to the outcome, provided sampling points lie exactly on the surface.

The final source of numerical instability is the computation of the Voronoi diagram. The precision of the Voronoi computation imposes a lower bound on the precision of our algorithm. Our Voronoi cells are typically long and skinny, as the vertices in 3D Euclidean space are restricted to positions on a 2D manifold S . Their width is of the order of the typical nearest-neighbour distance r of sample points on the surface S , whereas their length is of

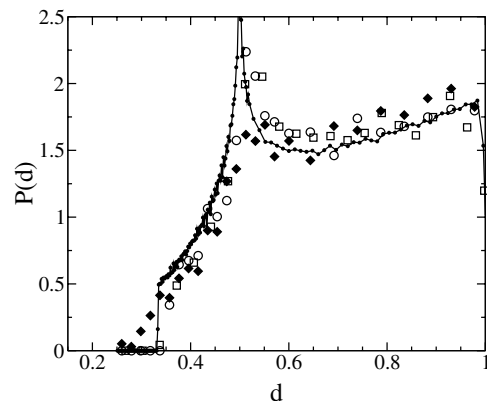


Fig. 5. Area weighted distance function distribution (see section 5 for the definition) for an ellipsoid given by $(x/3)^2 + (y/2)^2 + (z/1)^2 = 1$: Connected small black dots are data for a high-resolution ellipsoid (24000 vertices) for which the MS is computed by intersecting straight lines in surface normal direction with the $z = 0$ plane; large symbols indicate data computed with our algorithm. A relatively coarse triangulation ($n \approx 2200$ vertices) with (open circles) and without exact normals (open squares) and one with some noise in the surface coordinates (achieved by adding random numbers between $[-0.03l, 0.03l]$ where l is the average triangle edge length; filled diamonds).

Table 1. Crystallographic coordinates of minima, maxima and saddle points of d (coordinates), together with the point group symmetry of the site (Sym) and its Wyckoff symbol (Wyck). Crystallographic coordinates refer to the space group [29] of the domain C (*i.e.* the “black-white group” of the oriented surface). Corresponding absolute values of the distance function d and the radius $r_c = 1/\sqrt{-K}$ (where K is the Gaussian curvature) are listed, for unit cells of lattice parameter a (unit cells are scaled such that the three surfaces are isometric). The numerical values for coordinates are correct to ± 2 in the last given digit, unless otherwise indicated. The area of the asymmetric unit patch, A_0 , area-weighted average distance, $\langle d \rangle$, and the volume associated with the asymmetric unit patch, V_0 , are also listed (V_0 is the volume foliated by reduced parallel surfaces in positive normal direction from the surface, *i.e.* the volume on one side of the original surface). The surface coordinates are obtained from usual Weierstrass representation for minimal surfaces as in [20, 54] plus roto-translation in \mathbb{E}^3 . The functional form of the Weierstrass function $\exp(i\phi)(t^8 - 14t^4 + 1)^{-1/2}$ is the same for all three surfaces, with the Bonnet angle ϕ distinguishing the three cases. The complex variable w indicates the preimage in the complex plane of the respective points ($w_1 = (\sqrt{3} - 1)/\sqrt{2}$, $w_2 = (\sqrt{2} - 1)\exp(i\pi/4)$, $w_3 = 0.3178$, $w_4 = 0.2863$, $w_5 = (\sqrt{2} - 1)\exp(i3\pi/4)$, $w_6 = 0.3644\exp(i0.4177\pi)$, $w_7 = (\sqrt{2} - 1)\exp(-i\pi/4)$).

point	position on S				position on MS			d	r_c
	ω	Coordinates	Sym	Wyck	Coordinates	Sym	Wyck		
Primitive, $Pm\bar{3}m$, $a = 2.15652$, $\phi = \pi/2$, $A_0 = 0.2272$, $V_0 = a^3/(2 \times 48) = 0.104$, $\langle d \rangle = 0.60$									
$y_1 = 0.018$, $y_2 = 0.1751$, $x_1 = 0.3249$, $x_2 = 0.136$									
Max	w_1	$[\frac{1}{4}, \frac{1}{4}, \frac{1}{4}]$	$3m$	8g	$[0, 0, 0]$	$m\bar{3}m$	1a	0.9338	∞
Min	0	$[\frac{1}{2}, \frac{1}{4}, 0]$	$mm2$	12h	$[\frac{1}{2}, y_1, 0]$	$mm2$	12h	0.500	0.5000
S_1	w_7	$[\frac{1}{2}, y_2, y_2]$	$mm2$	12j	$[\frac{1}{2}, 0, 0]$	$4/mmm$	3d	0.5340	0.5774
S_2	w_2	$[x_1, x_1, 0]$	$mm2$	12i	$[x_2, x_2, 0]$	$mm2$	12i	0.577	0.5774
Diamond, $Fd\bar{3}m$ (origin at $\bar{4}3m$), $a = 3.37150$, $\phi = 0$, $A_0 = 0.2272$, $V_0 = a^3(2 \times 192) = 0.100$, $\langle d \rangle = 0.57$									
$z_1 = 0.1483$, $x_2 = 0.004$, $x_3 = 0.1846$, $z_3 = -0.0307$, $x_4 = 0.1129$, $x_5 = 0.1910$, $y_5 = -0.0247$									
Max_1	w_1	$[\frac{1}{8}, \frac{1}{8}, -\frac{1}{8}]$	$3m$	32e	$[0, 0, 0]$	$\bar{4}3m$	8a	0.730	∞
Min	0	$[\frac{1}{4}, \frac{1}{4}, 0]$	$2mm$	48f	$[\frac{1}{4}, \frac{1}{4}, z_1]$	$2mm$	48f	0.5000	0.5000
S_1	w_2	$[\frac{1}{4}, \frac{1}{8}, 0]$	2	96h	$[\frac{1}{8} + x_2, \frac{1}{8}, \frac{1}{8} - x_2]$	2	96h	0.5774	0.5774
S_2	w_3	$[x_3, x_3, z_3]$	m	96g	$[x_4, x_4, x_4]$	$3m$	32e	0.5929	0.6547
Max_2	w_4	$[x_5, x_5, y_5]$	m	96g	$[\frac{1}{8}, \frac{1}{8}, \frac{1}{8}]$	$\bar{3}m$	16c	0.5949	0.615
Gyroid, $I4_132$, $a = 2.65624$, $\phi \approx 38.015^\circ$, $A_0 = 0.4544$, $V_0 = a^3(2 \times 48) = 0.195$, $\langle d \rangle = 0.56$									
$x_1 = 0.124$, $y_1 = 0.700$, $z_1 = 0.176$, $z_2 = -0.064$, $x_3 = 0.3375$, $x_4 = 0.491$, $y_5 = -0.1625$, $y_6 = -0.311$									
Max	w_6	$[x_1, y_1, z_1]$	1	48i	$[\frac{1}{4}, \frac{5}{8}, 0]$	222	12d	0.609	0.683
S_1	w_1	$[0, \frac{1}{2}, 0]$	3	16e	$[\frac{1}{8}, \frac{5}{8}, -\frac{1}{8}]$	32	8b	0.575	∞
Min	0	$[0, \frac{3}{4}, \frac{1}{8}]$	2	24f	$[0, \frac{3}{4}, z_2]$	2	24f	0.500	0.5000
S_2	w_2	$[-\frac{1}{4} + x_3, \frac{5}{8}, \frac{1}{2} - x_3]$	2	24h	$[-\frac{1}{4} + x_4, \frac{5}{8}, \frac{1}{2} - x_4]$	2	24h	0.577	0.5774
S_3	w_5	$[\frac{1}{8}, 1 + y_5, \frac{1}{4} + y_5]$	2	24g	$[\frac{1}{8}, 1 + y_6, \frac{1}{4} + y_6]$	2	24g	0.558	0.5774

the order of the distance function value $d(p)$ and is not dependent on r . Particularly in the limit of small r , geometric degeneracies (more than four vertices on the surface of a sphere) or quasi-degeneracies occur which cause instabilities in the Voronoi computation. Detailed discussion of this issue can be found elsewhere; robustness of Voronoi computations is a well-studied problem [55], with a variety of established stable algorithms known for its solution [15, 24, 51].

Appendix A gives an analysis of the approximation of centers of curvature by local Voronoi cells in terms of curvature properties of the bounding surface. There, we also analyse the effects of a small degree of uncertainty in the surface normal direction.

MS of P, D and G surfaces

We have analysed in detail the MS structures of domains bounded by the three cubic genus-three IPMS, the P, D

and G surfaces. The domains C fill one of the two interwoven subspaces bounded by these surfaces, S . An exact integral representation of surface coordinates p in \mathbb{E}^3 as a function of the surface normal vector, $N(p)$ is possible (see *e.g.* [21]), using the Weierstrass equations for minimal surfaces. The vertex coordinates are produced by numerical integration of the Weierstrass equations. The resulting domains and their medial surfaces are shown in Figures 2, 3 and 4.

Crystallographic coordinates and symmetries of the critical points on the original surfaces and on the medial surfaces are shown in Table 1. The space group chosen is that for the orientable minimal surface, with the two medial surfaces unrelated by symmetry even if geometrically similar.

We note that these embedded IPMS divide space into two subvolumes and a single IPMS thus defines two domains. Two medial surfaces can therefore be traced.

Generic hyperbolic surfaces (*e.g.* the $I - WP$ triply periodic minimal surface) divide space into two morphologically distinct domains, and the pair of MS are symmetrically distinct. The subvolumes of our examples are symmetrically related to each other by translation (P and D) or inversion (G), in which case the MS on either side of these IPMS are likewise related.

4 Medial graphs from medial surfaces

Complex hyperbolic multi-handled surfaces, such as the IPMS discussed here, comprise interconnected networks of labyrinths. The introduction of a line graph, whose edges lie on labyrinth axes, allows a useful secondary descriptor of the global morphology of complex hyperbolic shapes. For example, “labyrinth graphs” have been discussed widely in the IPMS literature [19,33,39,59]. To date, rigorous definition of these graphs is lacking. Schoen described the labyrinth graph of IPMS as a pair of interpenetrating networks of tubes (presumably of infinitesimal radius) that, on inflation yield the IPMS as the surface common to both inflated labyrinths. This description, of qualitative merit, is not quantitative.

We note that the medial surface transform (MST) affords an optimal reduction of a 3D domain to a 2D skeleton that (together with the distance function) preserves all geometric shape information. Further reduction of the dimensionality to a 1D graph cannot, in contrast to the MST, offer a unique fingerprint of a generic domain C . C cannot be reconstructed from the medial graph except, where the medial surface itself degenerates to a 1D graph. In spite of that reservation, there remain compelling reasons to construct a graph that captures the locations and orientations of the labyrinths.

Attempts to compute medial graphs (also known as medial axes or skeletons) in voxelized data sets are numerous, see references [9,25,42,73] and references therein. Here we develop a corresponding algorithm for domains defined as above.

We propose the following reduction of the medial surface to a medial graph: The guiding idea is that the line graphs should be contained in the MS, follow paths of maximal distance function values and retain the topology and connectivity of the MS. We therefore define the line graph as the the map under ms of the ridge lines of the distance function profile on S , which can be determined by the following algorithm:

1. Determine all maxima $\{p_{max} \in S\}$ and saddle points $\{p_{sad} \in S\}$ of d .
2. Determine the paths $\mathcal{P} \subset S$ of steepest ascent starting at all saddle points. They necessarily end at maxima.
3. Use the map ms to map these paths \mathcal{P} onto the medial surface.

Step (1) requires care with regards to the detection of the critical points, particularly saddle points, of d . To avoid the complications of computing derivatives of the numerical function d defined on a triangulated surface, we have implemented the following process. We define a

circle $c_r(p)$, centered at $p \in S$ and oriented in positive sense around the normal $N(p)$, which is the intersection of a ball $B_r(p) \in E^3$ centered at p with the surface S . A maximum is a point p for which the distance function $d(p') - d(p)$ is negative for all $p' \in c_r(p)$ in the limit $r \rightarrow 0$. A saddle point is a point $p \in S$ for which $d(p') - d(p)$ as a function of $p' \in c_r(p)$ has more than two zeros in the limit $r \rightarrow 0$.

The medial graph one obtains from this algorithm contains a number of edges of lesser relevance to the labyrinth structure. These include edges which connect two maxima that are distinct on S , but collapse to a single point on the MS (*via* a saddle). An example is $Max \rightarrow S_2 \rightarrow Max$ on the P surface (Fig. 2). In addition, there may occur features contained in branch lines of the MS of the following type. The set of points p', p'' and $p''' \in S$ that map to a single location on the MS, $ms(p') = ms(p'') = ms(p''')$, may be of mixed character, with *e.g.* p' being a critical point whereas p'' and p''' are not. An example is the site S_3 on the gyroid (Fig. 4). In principle, medial graph edges passing through such points may be eliminated without loss of information regarding the labyrinth structure.

The features of our algorithm derive from the work of Bader [7], concerned with rigorous definitions of bonds in condensed molecular and atomic systems. Bader has studied the reduction of a (3D) spatial charge density field to a bonding network by integrating gradient fields of the charge density starting at saddle points. We can alternatively define the medial graph as the critical paths of a 3D (Euclidean) distance field $D : E^3 \rightarrow \mathbb{R}^+$, which assigns to each point in space the distance to the nearest point on S . The Euclidean distance field, D , has the peculiar property that its gradient is either of constant length 1 (and pointing away from the nearest surface point), or its gradient field is singular. Those singularities coincide exactly with the medial surface. Therefore, all critical points of D are located on the medial surface, and it is easy to verify that we detect all of them with our method. (Note that additional points, such as S_3 on the gyroid surface are also detected by our method.)

We have applied our medial graph algorithm to the simpler IPMS introduced above. The medial graphs for the P , D and G IPMS indeed contain Schoen’s “labyrinth graphs” as subgraphs [59]. Nodes of these medial graphs are either maxima of the distance function d (P and D surfaces) or, in the case of the Gyroid, saddle singularities of Hopf index -2 [34].

5 Homogeneity and packing frustration

The concept of *homogeneity* of surfaces embedded in 3D space was introduced to account for energy differences between “bicontinuous” surfactant-water mesostructures of various symmetries and topologies, modelled by IPMS [38,35]. The relevance of the P, D and G IPMS to bicontinuous mesophases is believed to be due to their almost uniform Gaussian curvature (compared with other IPMS). Local energetic contributions to stability, such as

the bending energy due to variations in the Gaussian curvature of IPMS, have been shown to favour the most symmetric (cubic) lowest genus IPMS (genus three) in the context of lipid-water self-assembly [22, 30, 38, 60]. It is certain however, that non-local interactions are also at work in these systems. For example, the P(imitive), D(iamond) and G(yroid) surfaces have *identical* curvatures for suitable scaling of their lattice parameters. All three IPMS are thus degenerate with respect to their bending energies. However, no more than two of these structures are formed in simpler molecular condensates (typically the D and G mesophases, more rarely the P) [71]. Differences in the global embeddings of the P, D and G surfaces in \mathbb{E}^3 point to the additional presence of a global “packing frustration” term stabilising these mesophases. Some attempts to incorporate these factors have been made taking into account chain stretching contributions [3, 18].

In particular, Duesing *et al.* offered some estimate of packing frustrations of the Diamond IPMS via estimates of distance variations from the labyrinth graph to the surface [18]. That measure is better determined *via* MS calculations.

Here we introduce an alternative notion of *global homogeneity* to quantify global differences, derived from the medial surface concept.

Homogeneity is the degree to which the volume elements dV (introduced in Sect. 2) vary in shape from one point on the surface to another. The degree of homogeneity is influenced by intrinsic surface properties (*e.g.* Gaussian curvature variations for surfaces of constant mean curvature such as IPMS) and by extrinsic features of the surface embedding in 3D space. We define a perfectly homogeneous structure to consist of identical volume elements. A hyperbolic and perfectly homogeneous form cannot be realised in \mathbb{E}^3 , as constant (negative) Gaussian curvature surfaces cannot be immersed in flat 3-space [31, 67]. A global tiling of \mathbb{E}^3 with identical volume elements induced by a hyperbolic surface is frustrated in \mathbb{E}^3 . All hyperbolic morphologies in \mathbb{E}^3 thus induce both stretching and bending contributions in their relative energies, due to that frustration. We quantify the degree of geometric frustration (the homogeneity) with the construction of volume elements, dV .

The volume elements consist of a stack of area elements, $da_r(p)$, of the parallel surfaces of S , at distance $r(p)$ from S , where $r(p)$ ranges from zero (on S) to $d(p)$ (on MS). The infinitesimal area element $da(p)$ is related to the curvatures of S at p and the area element on S :

$$da_r(p) = da(p)(1 + H(p)r + K(p)r^2/2). \quad (2)$$

Clearly, the curvature properties (and thus the bending properties) are identical for isometric surfaces. Hence, the distinction between their volume elements dV must be due to different lengths $d(p)$ of the volume elements. Those variations afford a useful measure of the (stretching) homogeneity differences between the P , D and G IPMS.

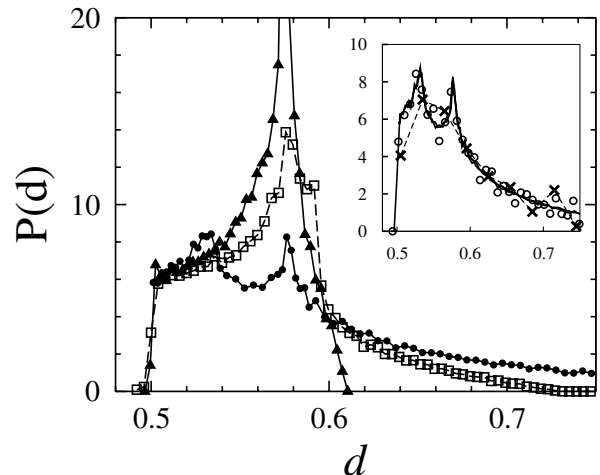


Fig. 6. Area weighted histogram of distances of isometric Primitive (disks), Diamond (squares) and Gyroid (triangles) surfaces. The cubic unit cell parameters are as indicated in Table 1. The data shown is for asymmetric unit patches with approximately 6000 vertices for the P and D surfaces, and 13000 vertices for the G (note that the G patch is twice as large as the P and D patch). The inset shows data for the P surface at different resolution: The data for 150000 and 8000 vertices (thin lines) is almost indistinguishable, data for 900 vertices (black dots) still resolves the bimodal nature of the distribution, whereas a surface patch with 100 vertices (crosses) correctly represents the overall tendency but not the bimodal distribution.

We have calculated an approximation to the distribution of distances

$$P(d) = 1/A \int_S da(p) \delta(d' - d(p)) \quad (3)$$

for those three IPMS, shown in Figure 6. Here A is the total area of the surface patch S which in the case of IPMS can be chosen to be an asymmetric unit patch of the (oriented) surface. The calculation is done as follows: Each vertex v of the representative asymmetric unit patch contributes $A_V(v)/A$ to the frequency where A is the total area of the asymmetric unit patch, and $A_V(v)$ the area of that part of the asymmetric patch which is contained in the Voronoi cell of vertex v . The data presented is for very fine discretizations, with approximately 6000 vertices for the P and D unit patch and 13000 vertices for the G unit patch (note that the asymmetric unit patch of the G is twice as large as for the P and D surface).

Additionally we show the effect of different levels of resolution (*i.e.* number of vertices per asymmetric unit patch) for the Primitive surface, with data sets of 150000, 6000, 800 and 100 vertices per unit patch. For the highest resolution, we take advantage of the fact that for the P surface, the medial surface can be computed by intersecting straight lines through surface vertices in normal direction with the global mirror planes. Each vertex v then contributes $A_T(v)/A$ to the frequency with $A_T(v)$ being the sum of the areas of all triangles of the asymmetric unit patch which share the vertex v .

Among those three surfaces (appropriately scaled to be isometric), the area-weighted distribution of radii, $d(p)$, is narrowest for the G IPMS, followed by the D and then P surfaces, see Figure 6. We conclude that the G IPMS is the least frustrated, most homogeneous spatial partition among these IPMS. Further, given the likely minimisation of intrinsic (Gaussian) curvature variations for the $P/D/G$ family compared with other lower symmetry or higher genus IPMS, the G IPMS is likely to be the most globally homogeneous hyperbolic partition of \mathbb{E}^3 among all IPMS.

6 Conclusions and outlook

The medial surface analysis presented in this article offers a mathematically sound approach to the characterisation of morphology of complex non-convex bodies such as intertwined channel systems which captures both local and global features of the structure. Most importantly, any surface element can be unambiguously associated with a corresponding volume element and a characteristic distance, offering a novel signature of spatial morphology.

The algorithm has proven to be suitable for high-precision computations of medial surfaces and medial graphs of topologically complex domains parametrised by exact mathematical formulae. It is shown to be robust with respect to small perturbations of the surface constrained to minimise curvature perturbations. Implementation for experimental data sets comprising polygonal surface data requires initial smoothing of the data to a designated curvature cutoff, to form a C^2 manifold [69,68]. The development of robust tools to compute medial surfaces of voxelized data sets to a desired resolution is an important next step.

The medial surface can be regarded as the endpoint of the reduced parallel surface transform: parallel surfaces overlap on the medial surface. This observation reveals the utility of the medial surface approach in many other applications. Mecke and colleagues have shown that analysis of parallel surfaces of sets of convex objects in terms of their Minkowski integrals (foliated volume, area, integrated mean curvature and Euler index) is a robust and physically relevant tool for spatial structure characterization [48], *e.g.* in the description of pore space morphologies in porous media [4] or reaction-diffusion systems [47]. The medial surface construction described here allows extension of the Minkowski integral geometric approach to non-convex objects of arbitrary complexity.

In the context of parallel surfaces, the medial surface is related to the concept of focal conic domains commonly invoked as a description for geometric defects in smectic liquid crystals (see [41] for an overview). A generic focal domain bears a close relation to the volume element, defined above. It consists of the foliation of parallel surfaces from both sides of a surface patch (S) to the focal surfaces of S . Focal conic domains are generated from patches S of Dupin cyclides, whose focal surfaces degenerate to a pair of 1D curves (Dupin's cyclide [32]). In that case, the

focal domains coincide exactly with the pair of volume elements from S . The volume elements therefore afford a natural generalization of focal conic domains to domains associated with layers of arbitrary geometry S . The MS patches corresponding to S define the locations of orientational defects for smectic domains due to lamellae lying in S .

A novel feature of our construction is the explicit association of cells that are subvolumes of the domain, $D' \subset D$, with patches of the domain's bounding skin, $S' \subset S$. Various assemblages of these cells can be used to derive novel (generically non-convex) polyhedral tilings of \mathbb{E}^3 . For example, if S' consists of a single asymmetric surface patch of the IPMS, the associated cell, D' affords a single-cell tiling of \mathbb{E}^3 , with S' as one of the faces. Pairs of these cells, sharing the S' faces, are prismatic tiles of \mathbb{E}^3 , with end-caps consisting of patches of the MS and with other (ruled) faces comprised of the normal bundle around the boundary of the asymmetric patch.

A similar construction to the latter example has been sketched for an idealised (and fictitious) constant (negative) curvature IPMS in \mathbb{E}^3 , giving a cell of tetrahedral aspect [40]. The ratio of the (minimal, bisecting) mid-surface to these ideal tetrahedra to the tetrahedral volume is exactly $4/3R$, where R denotes the magnitude of the radii of curvature of the homogeneous minimal surface. The analogous measures for the P, D and G domains are $1.263\langle r_c \rangle$, $1.318\langle r_c \rangle$ and $1.339\langle r_c \rangle$, respectively, where the average radius of curvature $\langle r_c \rangle = 0.8611$ (for the same lattice parameters as above) can be expressed as an integral in the complex plane (see [54], p. 144). This measure relates immediately to the dimensionless "shape parameter", commonly invoked to quantify the molecular shape in surfactant self-assembly [37,50].

Finally, we point out that the distance map induces a tiling on the domain skin S through the network of critical paths. Two such networks arise: one consisting of edges connecting saddle points to maxima and thus enclosing minima; the other connecting saddle points to minima, enclosing maxima. Faces of these networks can also be used as surface patches bounding volume elements, leading to a variety of cellular partitions of \mathbb{E}^3 , derived from domains of arbitrary topology, either open or closed. This might provide an extension to the Kelvin problem [44,70], which remains ill-defined if the cells are not closed [28].

We thank Klaus Mecke for fruitful discussions and advice. We acknowledge financial support through the Australian-German Joint Research Co-operation scheme (Adelaide University, ANU, AusIndustry and DAAD). CPU time was provided by the Australian Partnership for Advanced Computing.

Appendix A: Precision of the algorithm

In this appendix some issues related to the algorithmic stability of our MS computations are discussed. Note that this is a different issue from the geometric convergence problem dealt with by Amenta *et al.* and described in

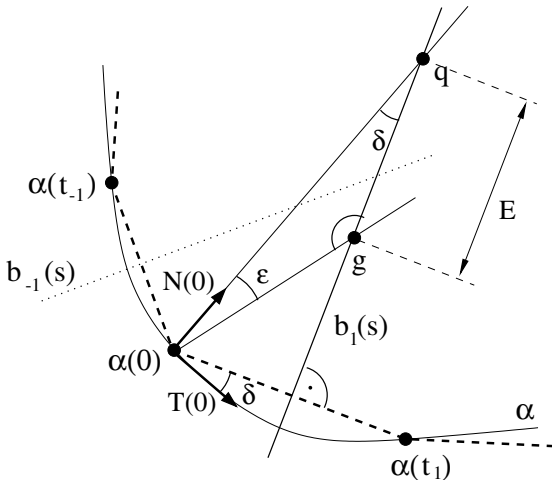


Fig. 7. Sketch of the 2D precision analysis. See text for details. Note that the discretization in this case is particularly bad to approximate the center of curvature, as the curvature properties of the edges (t_0, t_1) and (t_{-1}, t_0) are quite different from each other.

Section 3 of this article. Here, we estimate for the two-dimensional situation (1) the precision of the center of curvature approximation by intersecting local Voronoi cells with straight lines in normal direction, and (2) the influence of imprecision of the normal vector in this case. We then argue that the MS construction is most fragile in the situation where MS vertices correspond to centers of curvature. Therefore, the error analysis for the center of curvature approximation gives an upper bound on the error of the MS construction. Finally, an argument is presented mapping the 3D case onto 2D, thus allowing an estimate of the robustness of the MS algorithm discussed in this article.

We first establish the precision of the approximation of the center of curvature by intersections of local Voronoi cells with straight lines in normal direction: consider a cell $C \subset \mathbb{E}^2$ whose boundary is given by a unit-speed curve $\alpha: [-a, b] \rightarrow \mathbb{E}^2$, together with its normal field $N(a, b > 0)$. The real valued function $\kappa: [-a, b] \rightarrow \mathbb{R}$ measures the curvature of α . Also given is a discretization

$$\{\alpha(t_i) \mid -a = t_{-k} < \dots < t_{-1} < 0 = t_0 < t_1 < \dots < t_{n-k} = b\}$$

of the boundary α , see Figure 7.

The local Voronoi cell $V(0)$ of the three vertices $\alpha(t_{-1})$, $\alpha(0)$ and $\alpha(t_1)$ is bounded by the two perpendicular bisectors

$$b_i(s) = \alpha(0) + \frac{\alpha(t_i) - \alpha(0)}{2} + sJ\left(\frac{\alpha(t_i) - \alpha(0)}{2}\right) \quad (4)$$

where J denotes the counter-clockwise rotation in \mathbb{E}^2 , $i \in \{-1, 1\}$ and s is a real parameter defining the position on the bisector.

We now determine how well the intersection of the straight line through $\alpha(0)$ in normal direction $N(0)$ with the local Voronoi cell $V(0)$ approximates the center of curvature $\alpha(0) + 1/\kappa(0)N(0)$ in the case of positive curvature

at $t_0 = 0$. To this end we expand α in curvature terms at $t_0 = 0$.

Assuming sufficient smoothness and applying the Frenet formulae, a curve α can be expanded in terms of its curvature at $t_0 = 0$:

$$\alpha(t) = \alpha(0) + T(0) \left(t - \frac{\kappa(0)}{6}t^3 + \mathcal{O}(t^4) \right) + N(0) \left(\frac{\kappa(0)}{2}t^2 + \frac{\kappa'(0)}{6}t^3 + \mathcal{O}(t^4) \right). \quad (5)$$

Substituting the curvature expansion, equation (5), into the representation of the bisector, equation (4), and determining the intersection q of the bisector with the straight line in normal direction through $\alpha(0)$ one obtains

$$r_i = \frac{1}{\kappa(0)} \left(1 - \frac{\kappa'(0)}{3\kappa(0)}t_i + \mathcal{O}(t_i^2) \right) \quad (6)$$

for the distance $r_i = \|q_i - \alpha(0)\|$ between $\alpha(0)$ and the intersection q of the straight line in normal direction through $\alpha(0)$ with b_i .

The smaller of the two values r_{-1} and r_1 defines the radius of curvature at t_0 by the Voronoi intersection method. No distinction between the two values can be made by general consideration. Equation (6) represents the general precision for the approximation of the radius of curvature by intersecting straight lines in normal direction with the local Voronoi cell.

We now analyse the effect of uncertainty in the normal $N(0)$ on the position of the computed center of curvature g . Assume that the normal vector $N(0)$ is only known within an angle tolerance $\pm\epsilon$, see Figure 7. The estimate for the center of curvature deviate by a distance $E = \|q - g\|$ from the previously computed center of curvature q .

Consider the situation as shown in Figure 7: δ denotes the turning angle, i.e. the angle between the vector $\alpha(t_1) - \alpha(0)$ and the tangent $T(0)$ at $\alpha(0)$. This angle is the same as the angle formed by the straight line in normal direction through $\alpha(0)$ and the bisector $b_1(s)$. The angle δ is a simple integral of the curvature [27], and is given by

$$\delta = \int_0^{t_1} \kappa(t)dt = \kappa(0)t \left(1 + \frac{\kappa'(0)}{2\kappa(0)}t + \mathcal{O}(t^2) \right). \quad (7)$$

The distance $E = \|q - g\|$ is then related to the angles δ and ϵ and the computed radius of curvature $r_1 = \|q - \alpha(0)\|$ by

$$\frac{E}{r_1} = \frac{\sin \epsilon}{\sin(\pi - \delta - \epsilon)} \approx \frac{\epsilon}{\delta} \approx \frac{\epsilon}{\kappa(0)t}. \quad (8)$$

The approximation is valid if ϵ/δ , ϵ and δ are small.

For the approximation of the center of curvature by intersecting local Voronoi cells with straight lines in normal direction in 2D we conclude: (a) The approximation converges, and the error is linear in the quality of the discretization, measured in terms of κ'/κ . (b) Imprecision of

the curve normals leads to an error which is of the order of the maximal error in the normal angle compared to the turning angle per edge. If the error in normal angle is purely due to limited numerical precision whereas the turning angle remains small but finite, the error in the curvature center estimate is small. Discretizing almost flat parts of the curve with short edges leads to problems.

Medial surface points coincident with centers of curvatures (analysed in this Appendix) lead to the largest uncertainty. As is clear from Figure 7, uncertainty in normal directions is most significant in this case. The precision analysis presented here therefore represents an upper estimate for the errors.

The results described above are almost immediately applicable to the 3D case: For a given vertex $p \in S$, one now has to identify all n nearest neighbours $\{p_i \in S\}$ of p . Nearest neighbours in this context means all vertices $p \in V$ which are connected by an edge of the Delaunay triangulation to p and are close to p as measured along a path on S .

For each nearest-neighbour p_i one intersects the straight line in normal direction through p with the perpendicular bisector between p and p_i (which is in this case a plane containing the corresponding Voronoi facet). Again, the local Voronoi cell is defined as the set of perpendicular bisectors between p and all neighbouring points.

We define a planar curve α to be a unit speed curve lying within the intersection of S with a plane containing the surface normal $N(p)$, the point p and the point p_i . We define T_α as the tangent to α in p . The curvature of α at the point p is then (up to the sign) the normal curvature $\mathbf{K}_p(T_\alpha)$ of S in the direction of T_α , see Corollary 16.8 in [27]. Thus, the 2D analysis from above applies for the approximation of $\mathbf{K}_p(T_\alpha)$.

Intersecting all n nearest-neighbour Voronoi facets yields an approximation to the smallest of the positive radii of curvature (which is the relevant one for MS purposes). The quality of this approximation is then related to the curvature properties of curves $\alpha \subset S$ by the above 2D curvature analysis (effects of the neighbour vertices not sampling every direction from p are neglected).

References

1. N. Amenta, M.W. Bern, *Surface reconstruction by Voronoi filtering*, in *Symposium on Computational Geometry*, pp. 39–48 (1998)
2. N. Amenta, S. Choi, R. Kolluri, *Comput. Geometry: Theory and Applications*, **127**, 19 (2001)
3. D.M. Anderson, S.M. Gruner, S. Leibler, *Proc. Natl. Acad. Sci. USA* **85**, 5364 (1988)
4. C.H. Arns, *The influence of morphology on physical properties of reservoir rocks*, Ph.D. thesis, University of New South Wales, Australia, 2002
5. D. Attali, A. Montanvert, *Computer Vision and Image Understanding* **67**, 261 (1997)
6. F. Aurenhammer, *Computing Surveys* **23**, 345 (1991)
7. R.F.W. Bader, *Atoms in Molecules: a Quantum Theory*, Number 22 in “The International series of monographs on chemistry” 1st edn. (Oxford University Press, New York, 1990)
8. S. Bakke, P.-E. Øren, *Soc. Petroleum Engineers J.* **2**, 136 (1997)
9. I. Bitter, A.E. Kaufman, M. Sato, *IEEE Trans. Visualization and Computer Graphics* **7**, 195 (2001)
10. H. Blum, *J. Theor. Biol.* **38**, 287 (1973)
11. J.-D. Boissonnat, F. Cazals, *Natural coordinates of points on a surface*, In *Proceedings of the 16th Annual ACM Symposium on Computational Geometry*, pp. 223–232, 2000
12. H.I. Choi, S.W. Choi, H.P. Moon, *Pacific J. Mathematics* **181**, 57 (1997)
13. S.W. Choi, S.-W. Lee, *Stability analysis of the medial axis transform*, in *Proc. 15th International Conference on Pattern Recognition (Barcelona, Spain)*, Vol. 3, pp. 139–142, 2000
14. S.W. Choi, H.-P. Seidel, *Hyperbolic Hausdorff distance for medial axis transform*. MPI-I-2000-4-003, Research Report Max-Planck-Institut für Informatik, September 2000
15. K.L. Clarkson, K. Mehlhorn, R. Seidel, *Comput. Geometry: Theory and Applications* **3**, 185 (1993)
16. T. Culver, J. Keyser, D. Manocha, *Accurate computation of the medial axis of a polyhedron*, Technical Report TR98-038, UNC, 1999
17. T.K. Dey, W. Zhao, *Approximate medial axis as a voronoi subcomplex*, in *Proceedings of the seventh ACM symposium on Solid modeling and applications (ACM Press, 2002)*, pp. 356–366
18. P.M. Duesing, R.H. Templer, J.M. Seddon, *Langmuir* **13**, 351 (1997)
19. W. Fischer, E. Koch, *Acta Cryst. A* **45**, 726 (1989)
20. A. Fogden, S.T. Hyde, *Acta Cryst. A* **48**, 442 (1992)
21. A. Fogden, S.T. Hyde, *Acta Cryst. A* **48**, 575 (1992)
22. A. Fogden, S.T. Hyde, *Eur. Phys. J. B* **7**, 91 (1999)
23. F. Fol-Leymarie, *Three-Dimensional Shape Representation via Shock Flows*. Ph.D. thesis, Brown University, 2002
24. S. Fortune, *Voronoi diagrams and Delaunay triangulations*, in *Euclidean Geometry and Computers*, 2nd edn., edited by D.A. Du, F.K.H. Wang (World Scientific Singapore, 1995), pp. 193–233
25. N. Gagvani, D. Silver, *Parameter controlled skeletonization of three dimensional objects*. Technical Report, Computer Aids For Industrial Productivity, 1997
26. P. Giblin, B.B. Kimia, *Computer Vision and Pattern Recognition* **1**, 1566 (2000)
27. A. Gray, *Modern Differential Geometry of Curves and Surfaces with Mathematica* (CRC Press, 1998)
28. K. Grosse-Braukmann, *J. Colloid Inter. Sci.* **187**, 418 (1997)
29. *International Tables For Crystallography*, 3rd and revised edn., edited by T. Hahn (Kluwer Academic Publishers, Dordrecht, 1992)
30. W. Helfrich, H. Rennschuh, *J. Phys. Colloq. France* **51**, C7-189 (1990)
31. D. Hilbert, *Über Flächen von konstanter Gausscher Krümmung*, *Trans. A.M.S.* **2**, 87–99 (1901)
32. D. Hilbert, S. Cohn-Vossen, *Geometry and the Imagination* (Chelsea Publishing Company, New York, 1952)
33. D. Hoffman, J. Hoffman, M. Weber, The scientific graphics project, <http://www.msri.org/publications/sgp/sgp/main.html>

34. H. Hopf, *Differential Geometry in the Large*, Vol. 1000 of Lecture Notes in Mathematics. 2nd edn. (Springer-Verlag, 1989)
35. S.T. Hyde, S. Andersson, K. Larsson, Z. Blum, T. Landh, S. Lidin, B.W. Ninham, *The Language of Shape* (Elsevier Science B.V., Amsterdam, 1997)
36. S.T. Hyde, *Curr. Opin. Solid State Mater. Sci.* **1**, 653 (1996)
37. S.T. Hyde, *J. Phys. Chem.* **93**, 1458 (1989)
38. S.T. Hyde, *Curvature and the global structure of interfaces in surfactant-water systems*, *J. Phys. Colloq. France* **51**, C7 (1990)
39. S.T. Hyde, *Zeitschrift für Kristallographie* **187**, 165 (1990)
40. S.T. Hyde, S. Andersson, *Zeitschrift für Kristallographie* **168**, 221 (1984)
41. M. Kleman, O.D. Lavrentovich, *Soft Matter Physics: an Introduction* (Springer-Verlag, 2003)
42. Ta-Chih Lee, R.L. Kashyap, Chong-Nam Chu, *CVGIP: Graphical Models Image Processing* **56**, 462 (1994)
43. W. Brent Lindquist, Sang-Moon Lee, D.A. Coker, K.W. Jones, P. Spanne, *J. Geophys. Res.* **101**, 8297 (1996)
44. L. Kelvin, *On homogeneous division of space*, *Proceedings of the Royal Society, LV:1-17*, 1894
45. V. Luchnikov, N.N. Medvedev, L. Oger, J.P. Troadec, *Phys. Rev. E* **6**, 7205 (1999)
46. V. Luzzati, H. Delacroix, A. Gulik, T. Gulik-Krzywicki, P. Mariani, R. Vargas, *The cubic phases of lipid systems. physico-chemical properties and biological implications*, *Current Topics in Membranes*, Vol. 44, edited by R.M. Epand (Academic Press, 1997), pp. 3-24
47. K.R. Mecke, *Phys. Rev. E* **53**, 4794 (1996)
48. K.R. Mecke, *Additivity, convexity, and beyond: Applications of Minkowski functionals in statistical physics in Statistical Physics and Spatial Statistics - The Art of Analyzing and Modeling Spatial Structures and Patterns*, Vol. 554 of *Lecture Notes in Physics*, edited by K.R. Mecke, D. Stoyan (Springer Verlag, 2000), pp. 111-184
49. N.N. Medvedev, *Dokl. Akad. Nauk.* **337**, 767 (1994)
50. D.J. Mitchell, B.W. Ninham, *J. Chem. Soc. Faraday Trans. II* **77**, 601 (1981)
51. E. Muecke, *Int. J. Comput. Geometry Appl.* **8**, 255 (1998)
52. L.R. Nackman, *Comput. Graphics Image Processing* **20**, 43 (1982)
53. L.R. Nackman, S.M. Pizer, *IEEE Trans. Pattern Analysis and Machine Intelligence* **7**, 187 (1985)
54. J.C.C. Nitsche, *Vorlesungen über Minimalflächen* (Springer-Verlag, Berlin, Heidelberg, New York, 1975)
55. A. Okabe, B. Boots, K. Sugihara, Sung Nok Chiu, M. Okabe, *Spatial Tesselations: Concepts and Applications of Voronoi Diagrams*, 2nd edn. (John Wiley and Sons, 2000)
56. P.D. Olmsted, M.S.T. Milner, *Macromolecules* **31**, 4011 (1998)
57. F.P. Preparata, M.I. Shamos, *Computational Geometry* (Springer-Verlag, 1985)
58. E. Remy, E. Thiel, *Pattern Recognition Lett.* **23**, 649 (2002)
59. A.H. Schoen, *Infinite periodic minimal surfaces without self-intersections*. Technical report, NASA, 1970
60. U.S. Schwarz, G. Gompper, *Phys. Rev. Lett.* **85**, 1472 (2000)
61. U.S. Schwarz, G. Gompper, *Langmuir* **17**, 2084 (2001)
62. D. Shaked, A.M. Bruckstein, *Computer Vision and Image Understanding* **69**, 156 (1998)
63. D. Sheehy, C. Armstrong, D. Robinson, *IEEE Trans. Visualization and Computer Graphics* **2**, 61 (1996)
64. J.R. Shewchuk, *Discrete and Computational Geometry* **18**, 305 (1997)
65. R.M. Sok, M.A. Knackstedt, A.P. Sheppard, W.V. Pinczewski, W.B. Lindquist, A. Venkatarangan, L. Paterson, *Transport in Porous Media* **46**, 345 (2002)
66. E.H. Spanier, *Algebraic topology* (McGraw-Hill, 1966)
67. M.A. Spivak, *Comprehensive Introduction to Differential Geometry*, Vol. III (Wilmington, DE: Publish or Perish Press, 1979)
68. T. Tasdizen, R. Whitaker, P. Burchard, S. Osher, *Geometric surface smoothing via anisotropic diffusion of normals*, in *Proceedings of the conference Visualization '02* (IEEE Press, 2002), pp. 125-132
69. G. Taubin, *Curve and surface smoothing without shrinkage*, in *Proc. IEEE Int. Conf. Comput. Vision*, pp. 852-857, 1995
70. W. Thomson, *Acta mathematica* **1**, 121 (1888)
71. D.C. Turner, Z.-G. Wang, S.M. Gruner, D.A. Mannoek, R.N. McElhaney, *J. Phys. II France* **2**, 2039 (1992)
72. F.-E. Wolter, *Cut locus and medial axis in global shape interrogation and representation*. MIT design laboratory memorandum 92-2, MIT, 1992
73. Y. Zhou, A.W. Toga, *IEEE Trans. on Visualization and Computer Graphics* **5**, 196 (1999)